

# Demonstrating Single Photon Counting with Kinetic Inductance Detectors from 3.8 to 25 $\mu\text{m}$

Wilbert G. Ras-Vinke,<sup>1,2,\*</sup> Kevin Kouwenhoven,<sup>1,2</sup> Jochem J.A. Baselmans,<sup>1,2,3</sup>  
Kenichi Karatsu,<sup>1</sup> David J. Thoen,<sup>1,2</sup> Vignesh Murugesan,<sup>1</sup> and Pieter J. de Visser<sup>1,2</sup>

<sup>1</sup>*Space Research Organisation Netherlands (SRON), Niels Bohrweg 4, Leiden 2333 CA, Netherlands*

<sup>2</sup>*Department of Microelectronics, Delft University of Technology, Mekelweg 4, Delft 2628 CD, Netherlands*

<sup>3</sup>*Physikalisches Institut, Universität zu Köln, Zùlpicher Straße 77, 50937 Cologne, Germany*

(Dated: February 27, 2026)

One of the primary objectives of modern astronomy is the atmospheric characterization of Earth-like exoplanets at visible and infrared wavelengths. Achieving this goal requires extremely sensitive detectors capable of measuring the exoplanet’s faint signal at the single-photon level while maintaining near-zero dark count rates. In the infrared, however, conventional semiconducting detector technologies struggle to meet these stringent requirements. In this work we demonstrate single-photon counting with superconducting, Microwave Kinetic Inductance Detectors at the wavelengths 3.8, 8.5, 18.5 and 25  $\mu\text{m}$  and measure resolving powers ( $E/\delta E$ ) of 9.9, 5.9, 3.2 and 3.3, respectively, with corresponding dark count rates of 4, 8, 34 and 48 mHz. Our membrane-based devices reach phonon-loss limited performance at 3.8  $\mu\text{m}$ , more than doubling the performance attainable with comparable solid-substrate devices. These results showcase the detector technology in the mid-infrared and the intricate measurement setup required for these sensitive detectors. We discuss how the detector design and measurement setup can be further optimized to increase the detector performance in the mid-infrared.

## I. INTRODUCTION

Key to our understanding of life in the universe is the atmospheric characterization of Earth-like exoplanets to learn about their diversity, habitability and ultimately, whether they harbor life [2]. New ground- and space based observatories are currently in development that aim to do direct exoplanet imaging and spectroscopy in the visible to near-infrared (0.4  $\mu\text{m}$  to 2.5  $\mu\text{m}$ ) [3–8], as well as in the mid-infrared (mid-IR, 2.5  $\mu\text{m}$  to 30  $\mu\text{m}$ ) [9–11]. In this work we focus on the mid-IR wavelength range to address a gap in detector technology for these wavelengths.

The mid-IR is a scientifically valuable wavelength regime for a number of reasons. First, the mid-IR contains important absorption lines that are complementary to lines in the visible and near-IR and help constrain the atmospheric models. Second, the mid-IR offers a much more favorable (order 1000) star-planet contrast than the visible regime, alleviating the requirements on the optical system. Lastly, the planet’s brightness in the mid-IR puts better constraints on its temperature and radius. [12] However, the expected signal from such an exoplanet is so weak that it will require single-photon sensitive detectors with near-zero dark counts [13]. Conventional detectors based on HgCdTe, InAs/GaSb or Si:As technologies are unable to meet the required sensitivity in the mid-IR [14–16]. There are semiconductor-based detectors that reach single-photon sensitivity, but these do not cover the full mid-IR wavelength range [17–20].

Meanwhile, important progress has been made with

superconducting single-photon detectors for the mid-IR. Superconducting Nanowire Single-Photon Detectors [21] have demonstrated single-photon counting from the visible up to 29  $\mu\text{m}$  with dark counts below 100 mHz [15] and saturated internal detection efficiencies [16]. Microwave Kinetic Inductance Detectors (MKIDs) [22], on the other hand, have now demonstrated single-photon counting at 25  $\mu\text{m}$  with an optical efficiency of 46 % and dark count rate of 5 mHz [23]. MKIDs are superconducting detectors with a lot of heritage in astronomical application—both in the sub-mm to far-IR (2 mm to 0.03 mm) [24–26] and in the visible to near-IR [27]—due to their relative ease of multiplexing and fabrication. MKIDs for the sub-mm/far-IR are typically operated in a power-integrating mode with a lens-antenna structure to efficiently couple the light to the sensitive part of the detector, usually made of aluminium. However, the low resistivity of aluminium and limitations in fabrication technology make it progressively harder to achieve a high optical efficiency at shorter wavelengths. Creating periodic meandering absorbers from sub-micron wide thin aluminium can create a wideband absorber that is more robust to misalignment and assembly issues [28]. Such lens-absorber MKIDs have demonstrated single-photon detection at 25  $\mu\text{m}$  [23] and highly efficient power detectors at 43  $\mu\text{m}$  [28]. However, aluminium cannot be used to make an efficient detector in the visible/near-IR and is often replaced with higher resistivity superconductors, like beta-phase Tantalum, Hafnium or Titanium [29, 30]. Still, the highest energy resolving powers in the visible/near-IR have been achieved by suspending aluminium on a thin membrane [31]. The membrane reduces the loss of energetic phonons to the substrate which can increase the MKID’s energy resolving power—if it is phonon-loss limited—by a factor 2.4. Currently, energetic phonon-loss to the substrate is

\* Contact author at w.ras@sron.nl

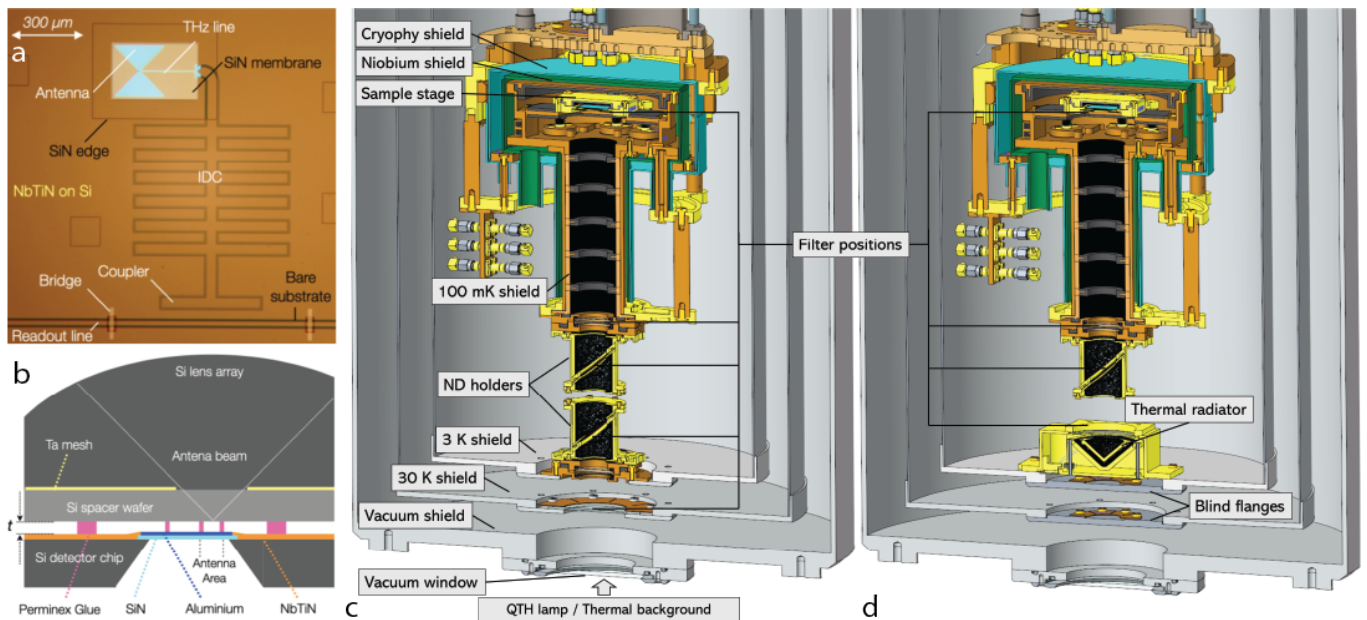


FIG. 1. MKID architecture and cryogenic setup. (a) Geometry of a single detector. The microwave resonator is made of a NbTiN IDC in parallel with aluminium CPW (THz line) with a highly inductive central line. The THz line is at the focus of a Si lens which is also the feed point of a leaky-slot antenna. The THz line is suspended on a SiN membrane to decrease phonon loss to the substrate. The detector design is originally optimized for the far-IR at  $200\ \mu\text{m}$ . (b) Cross-sectional view of the detector assembly. The figures in panels a and b are reproduced from Ref. [1]. (c) Cross section of the DR as configured for the experiments at  $3.8$  and  $8.5\ \mu\text{m}$  and (d) at  $18.5\ \mu\text{m}$ . The detectors are mounted at the sample stage. Indicated are the temperature shields as well as the Cryophy and Niobium magnetic shields. The key difference between the configurations is the source of radiation; (c) an external QTH lamp and (d) a cryogenic radiator at  $3\ \text{K}$ . Optical filters can be mounted at the indicated positions.

limiting the energy resolving power at  $25\ \mu\text{m}$  to  $2.9$  [23]. Phonon-trapping membranes will not give MKIDs the energy resolving powers required for spectroscopy, but the enhanced energy resolving powers will effectively reduce the detector's dark count rate by improving its ability to discriminate between in-band and out-of-band photons [32].

In this work we demonstrate single-photon counting with MKIDs on phonon-trapping membranes at  $3.8$ ,  $8.5$ ,  $18.5$  and  $25\ \mu\text{m}$ . We measure the energy resolving power at every wavelength and study its different contributions. We also describe and characterize the versatile and sensitive measurement setup that is required to facilitate single-photon counting across this wide wavelength range. The detector, measurement setup and pulse analysis are described in Sec. II. In Sec. III we present and discuss the results on the energy resolving powers and dark count rates. We summarize the outcomes and discuss future work in Sec. IV.

## II. METHODS

### A. Kinetic Inductance Detector

MKIDs are superconducting detectors, where photons with energy greater than twice the gap energy  $\Delta$  of the

superconductor can break Cooper pairs and change the complex impedance of a superconducting film. By integrating the superconducting film in a microwave resonance circuit, the change in impedance can be read out as a change of the complex  $S_{21}$  transmission at resonance [22].

The MKID array used in this work is identical to the one described in detail by Baselmans *et al.* [1]. Here we briefly reiterate the key design features with the single device architecture in Fig. 1(a,b) and the full array configuration in Fig. 8a. The array consists of 27 MKIDs. Each MKID consists of a niobium-titanium-nitride (NbTiN) interdigitated capacitor (IDC) and an aluminium coplanar waveguide (CPW) with a highly inductive central line; the THz line. The detector is capacitively coupled to the readout line at the IDC side and shorted at the end of the THz line. Radiation is coupled to the detector by a silicon (Si) lens that focuses the light onto the feed point of a leaky-slot antenna at the end of the THz line. Key is the suspension of the aluminium CPW on a  $\sim 100\ \text{nm}$  thick silicon-nitride (SiN) membrane for re-trapping of  $2\Delta$  phonons generated by quasiparticle recombination. The sensitivity and optical coupling have been optimized for the far-IR at  $200\ \mu\text{m}$ .

In this work we use the same detector at all wavelengths. The detector used has a  $0.773\ \mu\text{m}^3$  aluminium volume,  $4.60\ \text{GHz}$  resonance frequency,  $50\ \mu\text{s}$  quasiparti-

TABLE I. Optical filter configurations and radiation sources used for single photon counting at 3.8  $\mu\text{m}$ , 8.5  $\mu\text{m}$ , 18.5  $\mu\text{m}$  and 25  $\mu\text{m}$ . The filter positions at 3.8  $\mu\text{m}$ , 8.5  $\mu\text{m}$  and 18.5  $\mu\text{m}$  correspond to the DR setup seen in Fig. 1(c,d). The ADR setup at 25  $\mu\text{m}$  is described in Ref. [1] (Fig. 2c). For detailed descriptions of the filters, see Appendix A.

		3.8 $\mu\text{m}$	8.5 $\mu\text{m}$	18.5 $\mu\text{m}$	25 $\mu\text{m}$ (ADR)
<b>Filter positions</b>	<b>Sample</b>	$2 \times \text{BP}_{3.8} + \text{CaF}_2$	$2 \times \text{BP}_{8.5} + \text{CaF}_2$	$3 \times \text{BP}_{18.5}$	$\text{BP}_{25} + \text{SP}_B$
	100 mK	$\text{BP}_{3.8} + 2 \times \text{CaF}_2$	$\text{BP}_{8.5} + 2 \times \text{CaF}_2$	$\text{BP}_{18.5} + \text{ZnSe} + \text{ND}_1$	$\text{BP}_{25} + 2 \times \text{SP}_A$
	ND 100 mK	$\text{ND}_3$	$\text{ND}_3$	$\text{ND}_3$	-
	ND 3 K	$\text{ND}_2$	$\text{ND}_2$	-	-
	3 K	$\text{BP}_{3.8} + \text{CaF}_2$	$\text{BP}_{8.5} + \text{CaF}_2$	$\text{BP}_{18.5} + \text{ZnSe}$	$\text{BP}_{25} + \text{SP}_A + \text{LP}$
	30 K	$\text{CaF}_2$	$\text{CaF}_2$	Blind flange	-
<b>Source</b>		QTH lamp, external	Thermal background, external	Thermal radiator, at 3 K	Thermal radiator, at 3 K

cle lifetime (in dark conditions) and 2.3 meV energy resolution (from [1], Fig. 4d and Fig. B.1). This energy resolution promised the photon-counting ability in the mid-IR that has led to this work.

## B. Cryogenic setup and Microwave readout

A well controlled measurement setup is required to demonstrate single-photon counting with such a sensitive MKID detector. To have clearly distinguishable single-photons, the setup should allow the detector to see about 100 to 1000 photons per second; equivalent to 1 to 10 aW of power absorbed by the detector at 18.5  $\mu\text{m}$ . This requires an extremely light-tight setup as photons with an energy larger than the energy gap of aluminum (4 mm wavelength) can still break Cooper pairs in the detector.

The detector array is located at the sample stage of a Bluefors dilution refrigerator (DR) at a typical temperature of 100 mK. The cryostat is configured in one of two ways, see Fig. 1(c,d). The differences between the configurations will be discussed in more detail in Sec. II C, but the common elements are discussed here. The detectors are shielded from higher temperature environments by the 100 mK and subsequent 3 and 30 K shields. Shielding to external electric and magnetic fields are provided by a Cryophy and superconducting Niobium shield also at 100 mK. The 100 mK shield has a long snout containing a series of baffle rings for stray light control and the snout is also fully coated with a radiation absorbing layer of carbon-loaded epoxy with SiC grains [33]. A set of optical filters can be mounted at the indicated positions. The vacuum window is made from 6 mm thick  $\text{CaF}_2$  and is not considered as an optical filter as it is at ambient temperature. Dedicated neutral density (ND) filter holders have been designed to prevent standing waves between the filters. The holders tilt the ND filters at a 45° angle, reflecting the radiation to an absorbing layer that covers the inside. The ND holders can be mounted to the 100 mK and 3 K stages. The 25  $\mu\text{m}$  measurements are done in the adiabatic dilution refrigerator (ADR) from Ref. [1]. The configuration of the ADR is similar to the

DR configuration at 18.5  $\mu\text{m}$  (Fig. 1d) with a cryogenic radiator at 3 K. To measure the dark count rates we perform a multichannel dark count measurement in the DR which is described in more detail in Appendix B.

The microwave readout scheme used in this work is the same as the one described by Ref. [34] with the 2–6 GHz LNA. The response of the detector is the change in the in-phase and quadrature components of a readout tone centered on the equilibrium (dark) detector resonance. For single-photon pulse measurements we generally work with the phase response  $\theta$ , sampled at 1 MHz. The readout power  $P_{\text{read}}$  is optimized to just below the onset of bifurcation.

## C. Optical setup and characterization

We require different photon sources and filtering solutions to define the exact wavelength bands of interest at the desired power. In Fig. 1d we show the cryostat configuration at 18.5 and 25  $\mu\text{m}$ . The detectors are illuminated by a cryogenic radiator mounted on the 3 K stage that can be modeled as an ideal black body. The radiator can be heated by a resistor to temperatures up to 180 K without causing too much heat load on the 100 mK stage. Therefore, a different source is required at 3.8 and 8.5  $\mu\text{m}$ . The source at these wavelengths is external to the cryostat and illuminates the detector through a series of optical filters, Fig. 1c. This also means we have a thermal background present with a temperature of  $T_{\text{lab}} \approx 293$  K that peaks in radiance around 10  $\mu\text{m}$ . At 3.8  $\mu\text{m}$  we use a monochromator source: a 100 W Quartz Tungsten Halogen (QTH) lamp in series with a monochromator (Oriol Cornerstone™260) that spectrally filters the light using a tunable grating (model: 74080). The QTH lamp has no significant radiance at 8.5  $\mu\text{m}$  such that we only rely on the thermal background as our photon source.

We have summarized the filter configurations for the different wavelengths in Table I. Common to the filter stacks are the band-pass (BP) filters that transmit the desired wavelength and reject the background. The BP filters are mounted at multiple temperature stages to

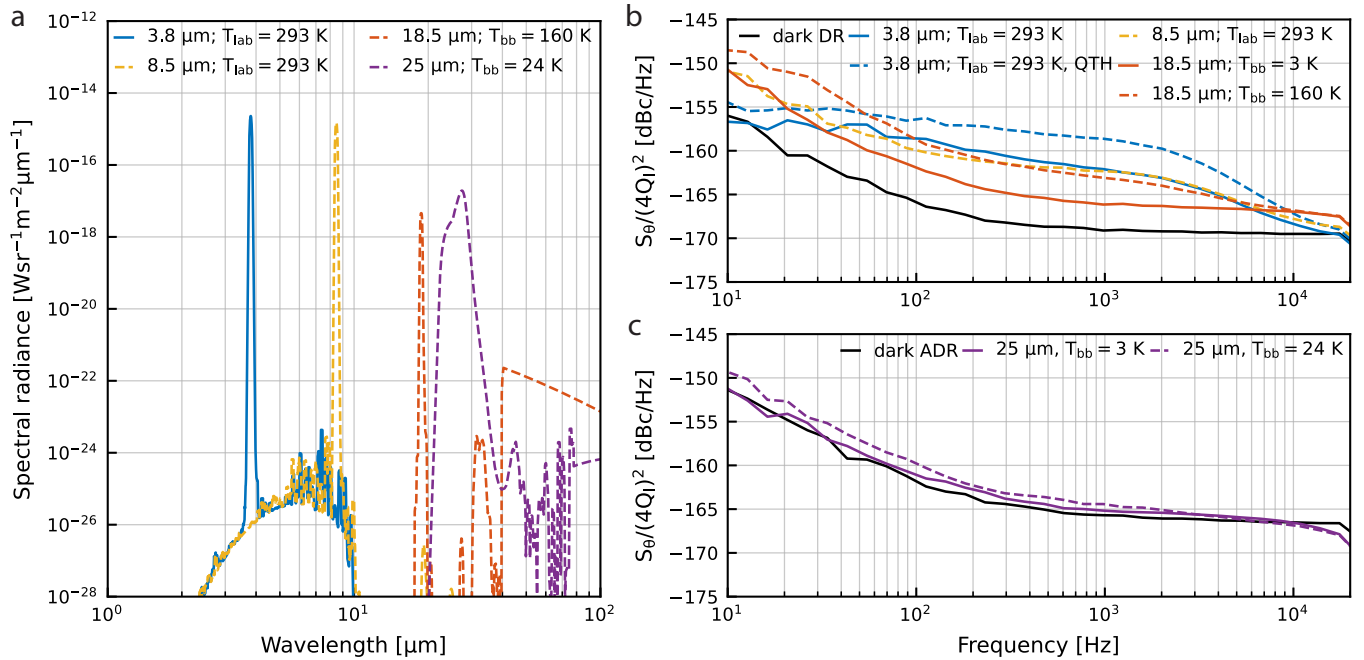


FIG. 2. Characterization of the measurement setups. (a) Estimated spectral radiance at the detector and (b,c) measured fractional frequency noise at 3.8, 8.5, 18.5 and 25 μm (blue, yellow, orange, purple, respectively) and in the dark (black). The 25 μm experiment was done in (c) the ADR, the others in the (b) DR. In all panels the solid lines represent the radiance and noise from just the background, while the dashed lines also include the radiation source.

reduce the effect of filter heating and re-radiation [35]. CaF<sub>2</sub> and ZnSe filters are added for short pass filtering and Neutral Density (ND) filters are used to reduce the power at the detector to acceptable levels. It is likely that some of the absorptive filters become increasingly transparent for the far-IR and longer wavelengths. In Appendix A we list the relevant characteristics of all the individual filters and provide relevant literature about their far-IR transmission.

We characterize the different measurement setups by computing the expected spectral radiance at the detector and by measuring the corresponding fractional frequency noise, see Fig. 2. The fractional frequency noise—hereafter denoted as *noise*—is computed from the power spectral density  $S_\theta$  and loaded quality factor  $Q_l$  of the resonator as  $S_\theta/(4Q_l)^2$ .  $S_\theta$  is computed from the resonator’s phase response with Welch’s method.  $Q_l$  is obtained from a Lorentzian fit to the MKID’s resonance dip. The fit incorporates both an asymmetric component according to Ref. [36, 37] as well as a non-linear component—as we operate near bifurcation—according to Ref. [38].

The expected spectral radiance  $I$  as a function of wavelength  $\lambda$  and black-body temperature  $T_{bb}$  is given by

$$I(\lambda; T_{bb}) = A\Omega B_\lambda(\lambda; T_{bb})\Theta(\lambda), \quad (1)$$

with  $A = \pi D^2/4$  the surface area of the lens (diameter  $D = 1.550$  mm),  $\Omega$  the solid angle of the limiting aperture in the setup ( $2^\circ$  in the DR,  $9^\circ$  in the ADR) and  $\Theta$  the total filter transmission. Lastly,  $B_\lambda$  is the black-body

radiance given by Planck’s law:

$$B_\lambda(\lambda; T_{bb}) = \frac{2hc^2}{\lambda^5} \frac{1}{e^{hc/(\lambda k_B T_{bb})} - 1}, \quad (2)$$

with  $h$ ,  $k_B$  and  $c$  physical constants. In Fig. 2a we have plotted the spectral radiance for every setup and in Fig. 2b we have plotted the corresponding noise levels. We observe the highest background noise at 3.8 μm (QTH lamp off) and the lowest at 18.5 and 25 μm ( $T_{bb} = 3$  K). We suspect far-IR radiation, transmitted through the filters, to cause the increased photon noise at 3.8 μm and, to a lesser extent, at 8.5 μm.

The 18.5 and 25 μm configurations have the lowest noise levels because a cryogenic source is used. However, there is a large difference in the required radiator temperatures: 160 and 24 K, respectively. The higher temperatures at 18.5 μm are due to the narrower 18.5 μm band pass filters, requiring higher radiator temperatures for the same in-band power. Consequently, there is much more background radiation ( $P \propto T^4$ ) present in the 18.5 μm setup which results in higher noise levels. Additionally, we expect the absorptive filters at 18.5 μm to be more transparent for the far-IR than the reflective filters used at 25 μm.

Additional characterization of the setup is done by measuring the photon count rate as a function of radiator temperature. No valid value for the optical efficiency can be extracted from this as it is nearly impossible to accurately model the optical efficiency of the lens-antenna structure of this detector in the mid-IR. Nonetheless, it

is insightful to check whether the detector and setup behave as expected. We model the absorbed photon count rate  $N_{\text{ph}}$  as a function of  $T_{\text{bb}}$  by integrating the radiance from Eq. (3) and dividing by the photon energy  $E_{\text{ph}}$ :

$$N_{\text{ph}}(T_{\text{bb}}) = \frac{\eta}{E_{\text{ph}}} \int_{\text{in-band}} I(\lambda; T_{\text{bb}}) d\lambda. \quad (3)$$

The *in-band* integration range is defined as the full width (99%) of the main transmission peak of the entire filter stack seen in Fig. 2a.  $\eta$  is the fitting parameter of our model and combines all the unknowns about the absorption mechanism of our detector in the mid-IR, including, but not limited to the optical efficiency. It is assumed that  $\eta$  is constant within the integration range.

#### D. Pulse detection and resolving power

A single-photon response of the detector is recognized in the time domain data by a fast rising edge followed by a slow exponential decay. Pulse detection is done in three steps. First, we remove noise spikes from the data using a three-point moving median filter. Second, we increase the signal-to-noise by smoothing the data with a falling exponential window that has a lifetime that is iteratively matched to that of the detected pulses. Last, we set a threshold for pulse triggering. We quantify the pulse detection thresholds in this work by means of the standard deviation of the smoothed noise,  $\sigma$ . Practically, the pulses are detected using the `scipy.signal.find_peaks` [39] module in Python with both the `height` and the `prominence` attributes set to the threshold value. Generally, we set the pulse detection threshold right at the noise floor,  $3\sigma$ .

After the pulses have been detected we want to find their pulse heights. The pulse-height distribution tells us about what type of pulses we have in our system and the spread of pulse heights determines the energy resolving power. The pulse heights in the presence of noise are most accurately estimated using an optimal filter constructed from the average pulse shape and average noise power spectral density (PSD) [40, 41]. The average pulse shape is constructed from a subset of all the detected pulses: the single-photon pulses from photon absorbed directly in the aluminium central line. We will explain this further Sec. III B. A single-photon pulse is defined as a pulse with no consecutive detections within a 400  $\mu\text{s}$  time window. The average noise PSD is constructed from a set of 400  $\mu\text{s}$  noise segments cut from the time stream in between the pulses.

The energy resolving power  $R = E/\delta E$  shows with what energy resolution  $\delta E$  the detector resolve the photon energy  $E$ . The response of the detector scales linearly with photon energy for the wavelengths measured in this work such that we can write  $R = \bar{H}/\delta H$  with  $\bar{H}$  average pulse height and  $\delta H$  the full-width-at-half-maximum of the pulse-height distribution. We estimate

$\delta H$  with a Kernel Density Estimate (KDE). We determine the resolving power for the same selection of pulses as used for the optimal filter. To characterize the detector and measurement setup we want to identify what the limiting contribution is to the resolving power. We define three possible contributions to the resolving power. First, the spectral (im)purity of the source and filter stack. This contribution is very small for the results of this work and neglected. The second contribution is the signal-to-noise ratio of the detector and readout chain,  $R_{\text{SN}} = \bar{H}/\delta H_{\text{noise}}$  with  $\delta H_{\text{noise}}$  the width of the optimally filtered noise. The last contribution is generally indicated as the *intrinsic* energy resolution and is obtained from the others  $1/R_i^2 = 1/R^2 - 1/R_{\text{SN}}^2$ . So,  $R_i$  includes all intrinsic effects that limit the resolving power, except for the detector noise. The ultimate limit to the resolving power is given by the statistical variation in the number of quasiparticles generated per photon; the Fano limit  $R_{\text{Fano}}$ . Device-specific limitations to the resolving power are captured by  $R_{\text{phonon}}$ ; a measure of how much the photon's energy is kept inside the detector and not lost by phonons that escape during the predetection stage[31].  $R_{\text{phonon}}$  is given by

$$R_{\text{phonon}} = \frac{1}{2\sqrt{2\ln 2}} \sqrt{\frac{\eta_{\text{pb}}^{\text{max}} E}{\Delta(F+J)}} \quad (4)$$

with  $E$  the photon energy and  $\eta_{\text{pb}}^{\text{max}} = 0.59$  the pair-breaking efficiency[42].  $F \approx 0.2$  is the Fano factor for superconductors [43, 44]. Note that  $R_{\text{Fano}} = R_{\text{phonon}}(J = 0)$ . Membrane devices thus have the potential to outperform devices on solid substrates by about a factor 2.4 in resolving power [31], but whether this also holds in the mid-IR is unknown.

### III. RESULTS

#### A. Single-photon detection across the mid-IR

In Fig. 3 the main result of this work is shown: single-photon pulses across the mid-IR. Visible are five 1 s time streams, starting on the left with the dark configuration and continuing to the right with the configurations at 3.8, 8.5, 18.5 and 25  $\mu\text{m}$ , respectively. We have smoothed the data with a falling exponential window with a lifetime that is approximately equal to that of the pulses. This differs between 50  $\mu\text{s}$  to 70  $\mu\text{s}$  between the configurations due to the different background loading. We also compensate for the difference in  $Q_l$  by rescaling the response at a wavelength  $x$  by a factor  $Q_l^x/Q_l^{\text{dark}}$ . At 3.8  $\mu\text{m}$  we clearly see the pulses disappear when the QTH lamp is turned off (gray line, offset by  $-0.5$  rad for visibility). Similarly, at 18.5 and 25  $\mu\text{m}$  the pulses disappear when the radiator is turned off. At 8.5  $\mu\text{m}$  we just see the photons that originate from the thermal background. In Fig. 4b we have plotted the mean pulse shape of the pulses at 3.8  $\mu\text{m}$  both on linear and semi-logarithmic scale

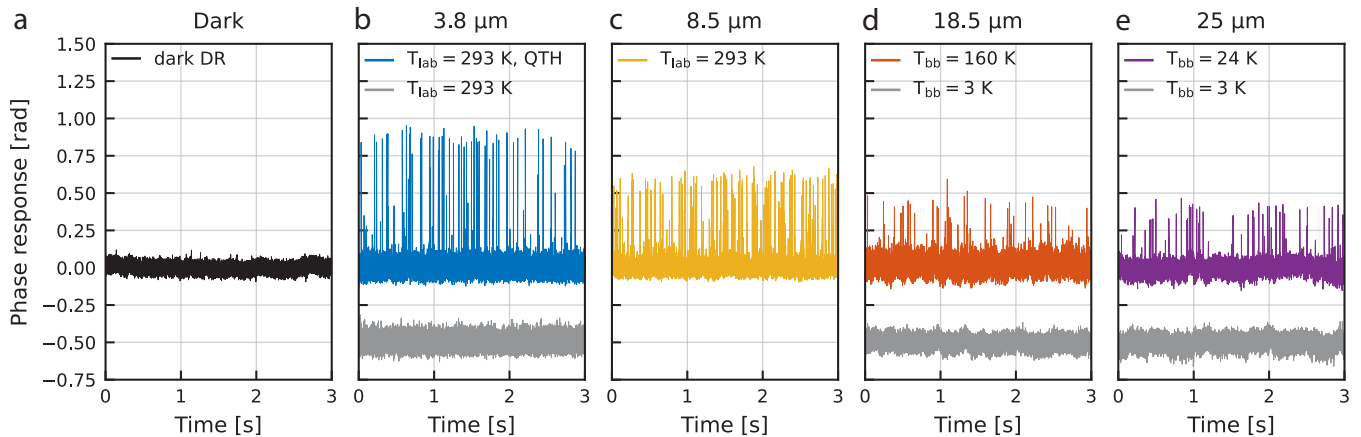


FIG. 3. Single-photon detection across the mid-IR. Shown are phase response time streams in the dark and at 3.8, 8.5, 18.5 and 25  $\mu\text{m}$  in panels *a-e*, respectively. At 3.8, 18.5 and 25  $\mu\text{m}$  we show the absence of pulses when the radiation source is turned *off* (gray line, offset by  $-0.5$  rad for clarity). At 8.5  $\mu\text{m}$  the radiation source is the every present thermal background of the lab. The data is smoothed with an exponential window with a lifetime of 50  $\mu\text{s}$ . We rescale the response at a wavelength  $x$  by a factor  $Q_1^x/Q_1^{\text{dark}}$ .

(inset). The quasi-particle lifetime  $\tau_{\text{qp}}$  of the pulse is obtained from fitting  $y = ae^{-x/\tau_{\text{qp}}}$  with  $a, b$  and  $\tau_{\text{qp}}$  the fitting parameters. We find  $\tau_{\text{qp}} = (55 \pm 1) \mu\text{s}$ .

## B. Energy resolving power

We investigate the MKID pulse detection performance in the mid-IR by measuring the energy resolving power and its contributions. We plot the optimally filtered noise and pulse-height distributions at 3.8, 8.5, 18.5 and 25  $\mu\text{m}$  in panels *a, c, d* and *e* of Fig. 4, respectively. We can distinguish three different pulse contributions: *direct*, *indirect* and *far-IR* pulses. These are most clearly observed at 3.8  $\mu\text{m}$  (Fig. 4a, annotations). The *direct* pulses are from single-photons absorbed in the aluminium central line and make up the primary distribution above 1 rad. The *indirect* pulses are from single-photons absorbed in the aluminium groundplane. These can lead to a pulse response in two ways: (1) the photon energy generates quasiparticles in the ground plane, creating a pulse with much smaller responsivity than a pulse from a photon absorbed in the central line; and (2) the photon energy is converted to phonons, which partially reach the central line and again lead to a pulse response, but with a smaller pulse height. The indirect pulses were also observed by Ref. [31] (Appendix B). The last pulse contribution is from the *far-IR* background that leads to a large number of detections just above the noise floor. When comparing the far-IR pulse contributions at all wavelengths one can see that it is smallest at 25  $\mu\text{m}$  (Fig. 4e). This is as expected from Fig. 2. The resolving power of the detector is determined from the direct pulses alone, as is the optimal filter. The direct pulses are selected by increasing the pulse detection threshold such that we remain only with the primary pulse-height distribution. The resolv-

ing power then is determined with a KDE. The KDEs for all the wavelengths are plotted in Fig. 4 with their corresponding pulse detection threshold indicated in the legends. Note that the detection threshold is set in the smoothed data, before optimal filtering; the optimal filtering transforms the hard cut in smoothed pulse heights into a gradual transition seen from the KDEs. This method enables us to determine the width—and thus resolving power—of the direct pulse distribution even when it is obscured by the indirect pulses, as is the case at 18.5  $\mu\text{m}$  (Fig. 4d).

The results of  $R$ ,  $R_{\text{SN}}$  and  $R_i$  at all wavelengths measured in this work are plotted in Fig. 5a. We also plot the phonon-limited resolving power  $R_{\text{phonon}}$  for a substrate ( $J = 3.1$ , dashed line) and membrane ( $J = 0.38$ , solid line) device, see also Sec. IID. The values for  $J$  are obtained in the visible/near-IR regime from Ref. [31] and extrapolated to the mid-IR (using  $T_c = 1.54$  K). Lastly, we plot the results from Ref. [23] at 25  $\mu\text{m}$ . At 3.8  $\mu\text{m}$  we find that  $R_i$  matches  $R_{\text{phonon}}$  for membrane devices. This indicates that phonon-trapping affects the resolving power at our mid-IR wavelengths in the same way as was found for higher energy photons, as expected. We do not reach phonon-loss limited performance at other wavelengths due to the indirect photon pulses broadening the direct pulse-height distribution. The large contribution of indirect detections is a consequence of the unoptimized optical coupling. While the detector intrinsically performs at its best at 3.8  $\mu\text{m}$ , the measurement setup seems to limit the resolving power. This is illustrated best when we extrapolate the  $R_{\text{SN}}$  found at 25  $\mu\text{m}$  to the lower wavelengths by rescaling with the photon energy, see the yellow, dash-dotted line in Fig. 5a. The line shows that we have the highest noise in the setup at 3.8  $\mu\text{m}$  which was also observed in Sec. IIC and attributed to the far-IR background.

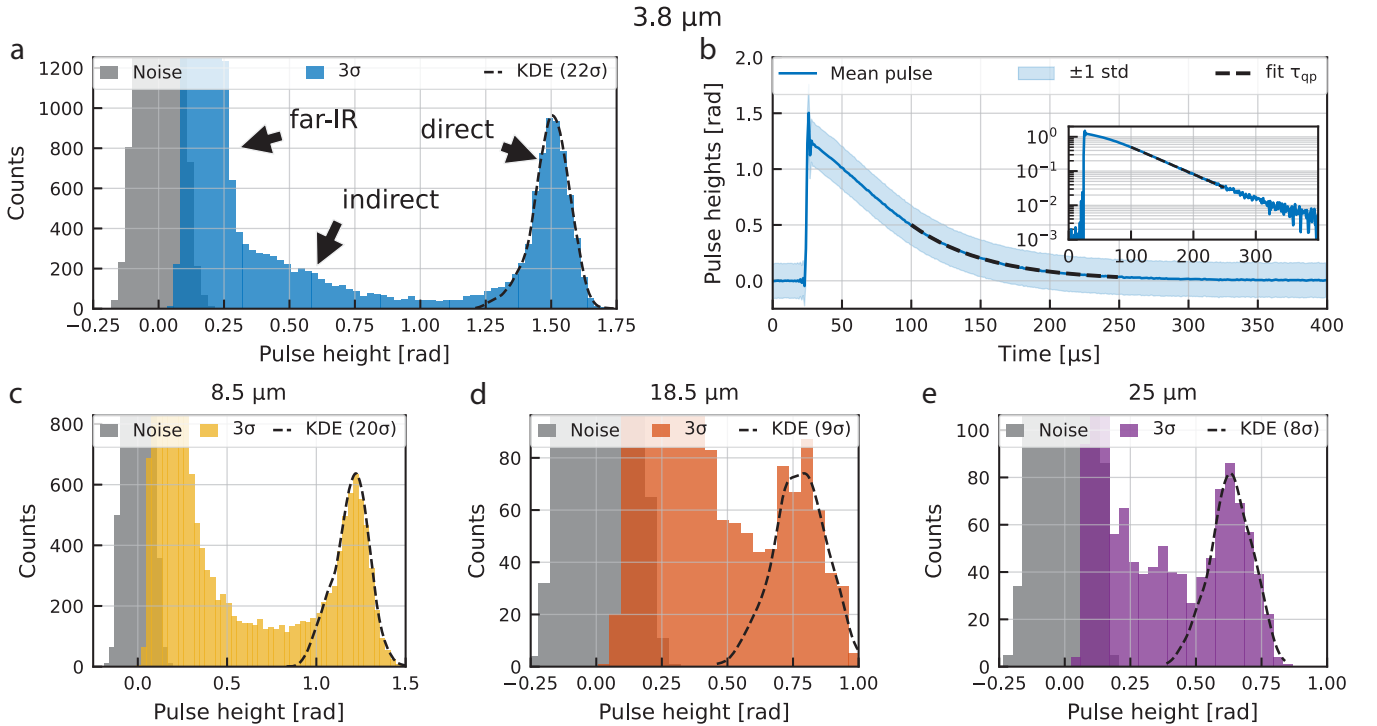


FIG. 4. Energy resolving power in the mid-IR. Optimally filtered noise (gray shaded) and pulse-height distributions at (a, blue shaded)  $3.8\ \mu\text{m}$  (c, yellow shaded)  $8.5\ \mu\text{m}$  (d, orange shaded)  $18.5\ \mu\text{m}$  and (e, purple shaded)  $25\ \mu\text{m}$ . We have annotated three different pulse contributions in panel *a* which are explained in main text. The pulses are detected with a  $3\sigma$  threshold in the smoothed data and then cut from the raw data before being optimally filtered. The optimal filter is constructed from the pulses in the primary distribution which is identified by the KDE (black, dashed line) and obtained by increasing the detection threshold to the level in the legend. The resolving power is then determined for the same selection. We rescaled the pulse heights at a wavelength  $x$  by a factor  $Q_1^x/Q_1^{\text{dark}}$ . (b) The average pulse shape of the directly absorbed  $3.8\ \mu\text{m}$  photons (indicated by the KDE in panel *a*), both on a linear and semi-logarithmic scale (inset). The shaded region indicates the  $\pm 1$  standard deviation from the average pulse shape. An exponential decay fitted to the tail of the pulse (black, dashed line) gives a  $\tau_{\text{qp}} = (55 \pm 1)\ \mu\text{s}$ .

### C. Dark count rate

We have measured the dark count rate for the detector, see Fig. 5b. The dark count measurement and analysis are described in Appendix B. We use the energy resolving power to discern a dark count rate per wavelength and find values of 4, 8, 35 and 48 mHz at the wavelengths of 3.8, 8.5, 18.5 and  $25\ \mu\text{m}$ , respectively. These values are determined with the resolving power of the detector at every wavelength and by requiring a 99.73% (i.e.  $\mu \pm 4\sigma$  or  $\bar{H} \pm 1.7\delta H$ ) confidence to detect all the direct single-photon pulses. A higher resolving power will lower the dark count rate further: a phonon-loss limited resolving power for a membrane device at  $18.5\ \mu\text{m}$  would lead to dark count rates of around 5 mHz instead of 20 mHz in our current setup.

Lastly, we validate the behavior of the detector and measurement setup at  $18.5\ \mu\text{m}$ , see Fig. 6. We measure the number of direct photon pulses versus radiator temperature using the  $9\sigma$  detection threshold also used in Fig. 4d. The model from Eq. (3) fits very well to the measured photon rates  $N_{\text{ph}}$  at  $T_{\text{bb}} \geq 85\ \text{K}$  using a sin-

gle fitting parameter  $\eta = (7.8 \pm 0.2) \times 10^{-2}$ . We have included the transmission of the Si lens into this calculation which is around 0.2 at  $18.5\ \mu\text{m}$ , see Fig. 7b (from Ref. [45]).

## IV. CONCLUSIONS

We have demonstrated single-photon counting at 3.8, 8.5, 18.5 and  $25\ \mu\text{m}$  using an MKID with aluminium on a thin membrane. At every wavelength a dedicated setup was designed, utilizing different radiation sources and filter configurations to cover the broad range of wavelengths. We measured energy resolving powers  $R$  of 9.9, 5.9, 3.2 and 3.3, respectively. With these resolving powers we obtained dark count rates of 4, 8, 35 and 48 mHz, respectively, from a 10000 s dark measurement.

Higher resolving powers are desirable to reduce the dark count rates of the detector. We reach phonon-loss limited performance at  $3.8\ \mu\text{m}$  and we believe this performance can be matched across the mid-IR, outperforming similar solid substrate devices by about a factor 2.4

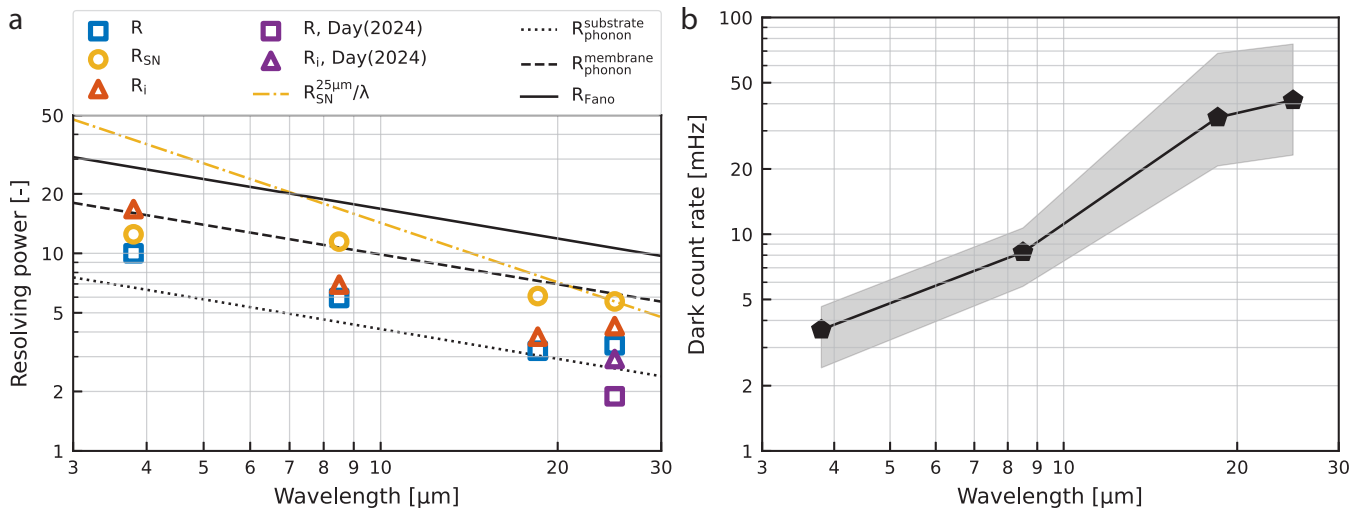


FIG. 5. Energy resolving powers and dark count rates at 3.8, 8.5, 18.5 and 25  $\mu\text{m}$ . (a) Plotted are the energy resolving power  $R$  and the signal-to-noise  $R_{\text{SN}}$  and intrinsic  $R_i$  contributions (blue, yellow and orange markers, respectively) that were obtained at 3.8, 8.5, 18.5 and 25  $\mu\text{m}$ . We plot the Fano limit from Eq. (4) (black, solid line,  $J = 0$ ) and the phonon-loss limited resolving powers for solid-substrate ( $J = 3.1$ ; black, dotted line) and membrane devices ( $J = 0.38$ ; black, dashed line). We extrapolate the  $R_{\text{SN}}$  at 25  $\mu\text{m}$  to the other wavelengths by scaling with  $\lambda$  (yellow, dash-dotted line). We also plot  $R$  and  $R_i$  obtained by Ref. [23] at 25  $\mu\text{m}$  (purple markers). (b) Dark count rates obtained from a 10 000 s measurement, see also Appendix B. The dark count rate are calculated per wavelength using the pulse-height distributions in Fig. 4 and a 99.73 % ( $\mu \pm 4\sigma$  or  $\bar{H} \pm 1.7\delta H$ ) confidence interval. The shaded area gives the 95.45 % ( $\mu \pm 3\sigma$ ) to 99.99 % ( $\mu \pm 5\sigma$ ) confidence range.

[31]. We have investigated the current limitations to the resolving powers measured in this work. At 3.8  $\mu\text{m}$  we are limited by an excess far-IR background in the setup. This is not surprising as we are exposing a single-photon sensitive detector to a 293 K thermal environment that

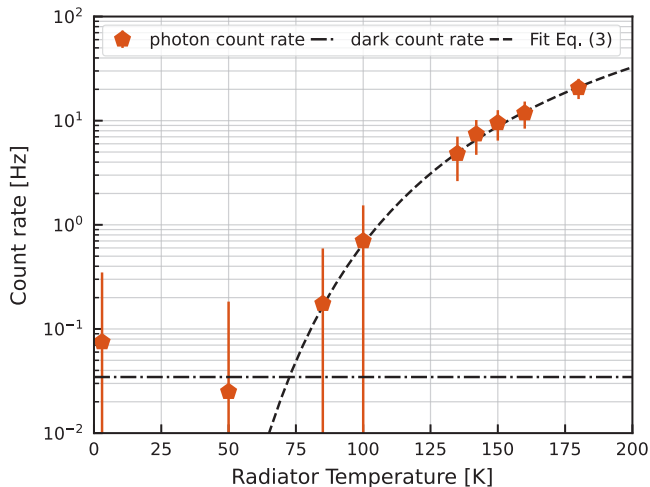


FIG. 6. Photon count rates  $N_{\text{ph}}$  versus radiator temperature  $T_{\text{bb}}$  at 18.5  $\mu\text{m}$ . The photon count rate is obtained from 40 s measurements. A  $9\sigma$  detection threshold was applied to only detect direct photon pulses, see also Fig. 4d. No photons were detected at 30 K. The error bars are given by the square root of the mean. We fit Eq. (3) to the data at  $T_{\text{bb}} \geq 85$  K and find  $\eta = (7.8 \pm 0.2) \times 10^{-2}$ . We plot the dark count rate from Fig. 5b at 18.5  $\mu\text{m}$  to show consistency.

requires—even in-band—more than 50 dB attenuation. The background radiation can be decreased by adding metal-mesh short pass filters or by using a cryogenic source like mid-IR Quantum Cascade Lasers [46]. At 8.5, 18.5 and 25  $\mu\text{m}$  we are limited by pulses from photons absorbed in the aluminium ground plane. This can be eliminated in future devices by using a lens-absorber coupling structure that is optimized for the mid-IR [23, 28]. This will likely require an optimized absorber per spectral channel as the mid-IR spans a factor 4 in wavelength. Besides, at 18.5  $\mu\text{m}$  the far-IR background should also be reduced by using broader band pass filters such that lower radiator temperatures can be used while having the same in-band power. To conclude, phonon-loss limited performance with membrane MKIDs is within reach across the mid-IR. This will enable single-photon counting with extremely low dark count rates across the mid-IR.

**Data and code availability** The raw data and code are made available on Zenodo to reproduce all the results in this work: <https://doi.org/10.5281/zenodo.18714817> and <https://doi.org/10.5281/zenodo.18714481>, respectively.

## ACKNOWLEDGMENTS

This work is financially supported by the Netherlands Organisation for Scientific Research NWO (Vidi 213.149 and OCENW.M.23.028). We would like to thank Nick de Keijzer for designing adjustments to the setup for this experiments, and the SRON workshop for producing those.

## Appendix A: Optical filters

Here we provide more detailed information on the specific filters used in the various measurement setups. In Fig. 7 the transmission curves of all the individual filters are shown and in Table II further specifications are listed. Based on literature we make an upper bound estimation for the optical transmission of the filters in the wavelength region not characterized by the manufacturer, up to  $100\ \mu\text{m}$ . The consulted literature is indicated in the row *Estimated FIR transmission* in Table II.

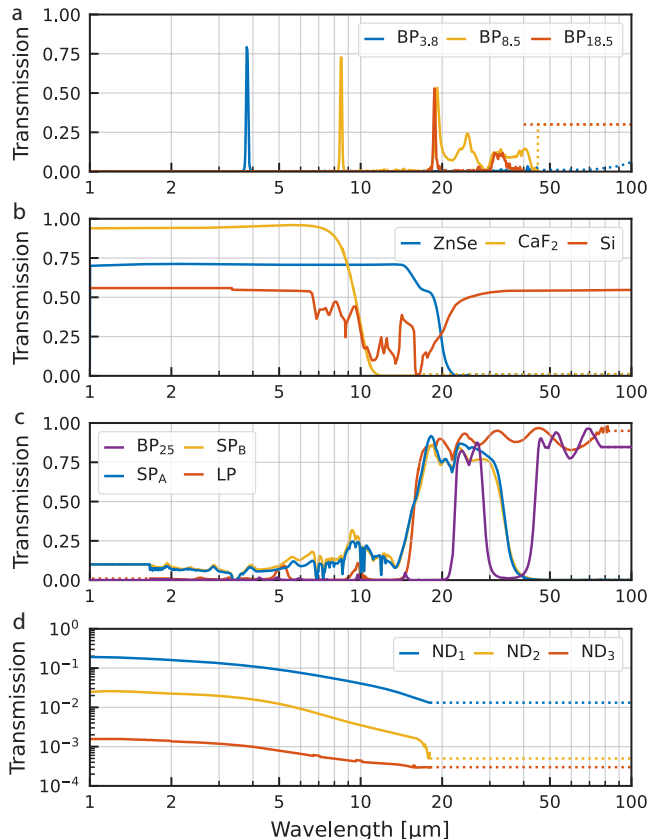


FIG. 7. Transmission spectra of the filters used in the various measurement setups. The dotted parts of the spectra indicate the wavelength regions where the filter has not been characterized. Outside of the characterized region we estimate a worst-case transmission based on literature.

## Appendix B: Dark counts

We want to minimize the effect of cosmic rays to obtain an accurate estimate of the detector dark count rate. The energy resolving power of the MKIDs enables rejection of the primary, high energetic events based on their pulse height. However, the deposited energy of the primary event can spread across the array during its down conversion process, leading to secondary detections in other detectors that could be indistinguishable from single photon pulses. Therefore, we do a simultaneous measurement of 7 detectors and reject all coincident events; events that occur within  $40\ \mu\text{s}$  across multiple detectors, similar to Ref. [23]. The multichannel measurement is done in the DR setup in the dark configuration, see also Sec. II. At a sampling rate of 1 MHz the readout was limited to a set of 7 detectors at the highest resonance frequencies (4.39 GHz to 4.60 GHz) which includes the detector analyzed in the main text. The detectors were measured simultaneously for a duration of 10 000 s. The detectors are spatially distributed over the whole array, with some being nearest neighbors and others spaced further apart, see Fig. 8a. One detector produced unusable data, but its individual location is unknown due to possible swapping of the resonances. The remaining 6 detectors are analyzed identically and in the same way as the detector in the main text, see Sec. IID. We set a pulse detection threshold of  $5\sigma$  to include all direct detections as well as many indirect detections (from cosmic rays), see Fig. 4. We find 25 coincident detections that occurred in 8 separate events. This is a negligible amount of the total number of detections and hardly influences our dark count rates. The highly suppressed effect of cosmic rays was also observed by Ref. [47] for a similar device with an aluminium groundplane on a membrane. The suppressed effect of cosmic rays probably limits our dark count rates because it rarely leads to a coincident event. For the detector analyzed in the main text we remove 8 detections out of 12 843. We optimally filter the dark counts using the same pulse template as used for the resolving power but with the noise from the dark measurement. The dark count rates are calculated per wavelength by setting a confidence interval for the pulse height based distributions of directly absorbed photons in Fig. 4. The confidence interval gives the probability of including all the single-photons that were detected at that wavelength. The confidence interval is calculated on the mean and FWHM of the pulse height distributions shown in Fig. 4. A 99.73% (i.e.  $\mu \pm 4\sigma$ ) confidence interval equals  $\bar{H} \pm 1.7\delta H$ . The dark count rates are given in Fig. 5b.

[1] J. Baselmans, F. Facchin, A. P. Laguna, J. Bueno, D. Thoen, V. Murugesan, N. Llombart, and P. De Visser, Ultra-sensitive THz microwave kinetic inductance detec-

tors for future space telescopes, *Astronomy & Astrophysics* **665**, A17 (2022).

TABLE II. Specifications of all the filters used in this work.

	BP <sub>3.8</sub>	BP <sub>8.5</sub>	BP <sub>18.5</sub>	BP <sub>25</sub>	CaF <sub>2</sub>	ZnSe	ND <sub>(1/2/3)</sub>	SP <sub>(A/B)</sub>	LP	Si
Manufacturer	NOC <sup>a</sup>	NOC <sup>a</sup>	NOC <sup>a</sup>	QMC <sup>b</sup>	EKSMA <sup>c</sup>	Thorlabs <sup>d</sup>	Thorlabs <sup>d</sup>	QMC <sup>b</sup>	QMC <sup>b</sup>	Veldlaser <sup>e</sup>
Part number	NC-2117	NC-2118	NC-2444-1	FP3223	530-6251	WG70530	NDIR(10/20/30)B	FP3238/FP3251	FP3253	-
Type	NBP <sup>f</sup>	NBP <sup>f</sup>	NBP <sup>f</sup>	BP <sup>g</sup>	SWP <sup>h</sup>	SWP <sup>h</sup>	ND <sup>i</sup>	SWP <sup>h</sup>	LWP <sup>j</sup>	Lens
cw <sup>k</sup> /fwhm <sup>l</sup> (μm)	3.8/76	8.5/170	18.5/370	25/6300	-	-	-	-	-	-
Cut-on (μm)	-	-	-	36	-	-	-	-	14	-
Cut-off (μm)	-	-	-	-	10	22	-	50	-	-
Thickness (mm)	1.0	1.0	1.0	<1	1.0	3.0	1.0	<1	<1	<sup>m</sup>
Diameter (mm)	25.4	25.4	25.4	25.4	25.4	25.4	25.4	25.4	25.4	1.550 <sup>n</sup>
Substrate	SiO <sub>2</sub>	Ge	Ge	°	CaF <sub>2</sub>	ZnSe	ZnSe <sup>p</sup>	°	°	Si
Char. temp. (K)	77 <sup>q</sup>	77 <sup>q</sup>	77 <sup>q</sup>	Room	Room	Room	Room	Room	Room	10
Char. band (μm)	0.8 – 45	0.8 – 45	0.8 – 40	1.7 – 77	0.2 – 16	1 – 25	0.2 – 18	1.7 – 77	1.7 – 82	3 – 100
Estimated THz transmission	λ > 100 μm [48]	λ > 45 μm [49]	λ > 40 μm [49]	extrapolated <sup>r</sup>	0.5 for λ > 200 μm [50]	0.01 [51]	extrapolated <sup>r</sup>	extrapolated <sup>r</sup>	extrapolated <sup>r</sup>	0.55 [45]

<sup>a</sup>: Northumbria Optical Coatings ltd; <sup>b</sup>: QMC Instruments ltd; <sup>c</sup>: EKSMA Optics; <sup>d</sup>: Thorlabs, Inc.; <sup>e</sup>: Veld Laser Innovations BV; <sup>f</sup>: narrow band pass; <sup>g</sup>: band pass; <sup>h</sup>: short wave pass; <sup>i</sup>: neutral density; <sup>j</sup>: long wave pass; <sup>k</sup>: central wavelength of the pass band; <sup>l</sup>: full width at half maximum of the pass band; <sup>m</sup>: lenses are elliptically shaped; <sup>n</sup>: diameter of single lens; <sup>o</sup>: the filter is composed of a stack of thin Copper meshes; <sup>p</sup>: The ZnSe substrate is covered with a thin Nickel film; <sup>q</sup>: characterized in-band at 77 K, out-of-band at room temperature; <sup>r</sup>: the last value of the characterized band is taken as the transmission at longer wavelengths;

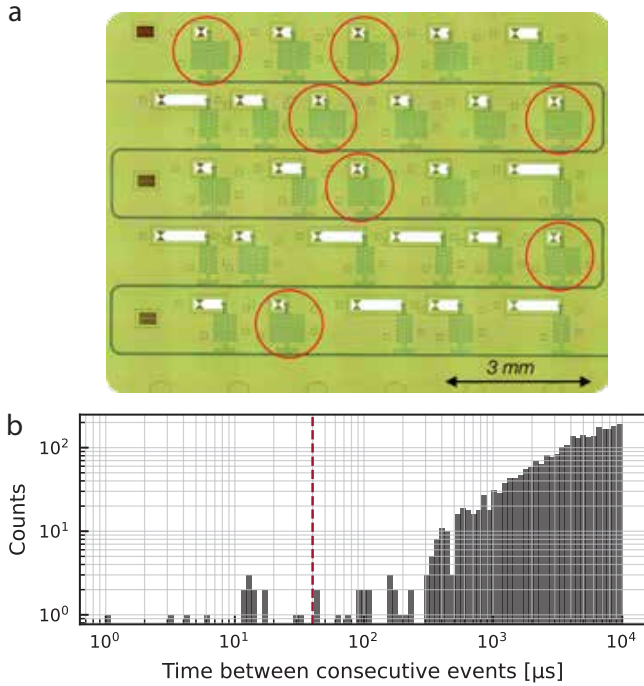


FIG. 8. Coincidence triggering. (a) Spatial configuration of the 7 detectors used for the coincident triggering. One detector produced unusable data. (b) Time difference between consecutive events of all detector that were detected during a 10000s measurement. A threshold of 40 μs yields only 8 coincident events leading to a total of 25 detections across all detectors (< 0.1% of all events)

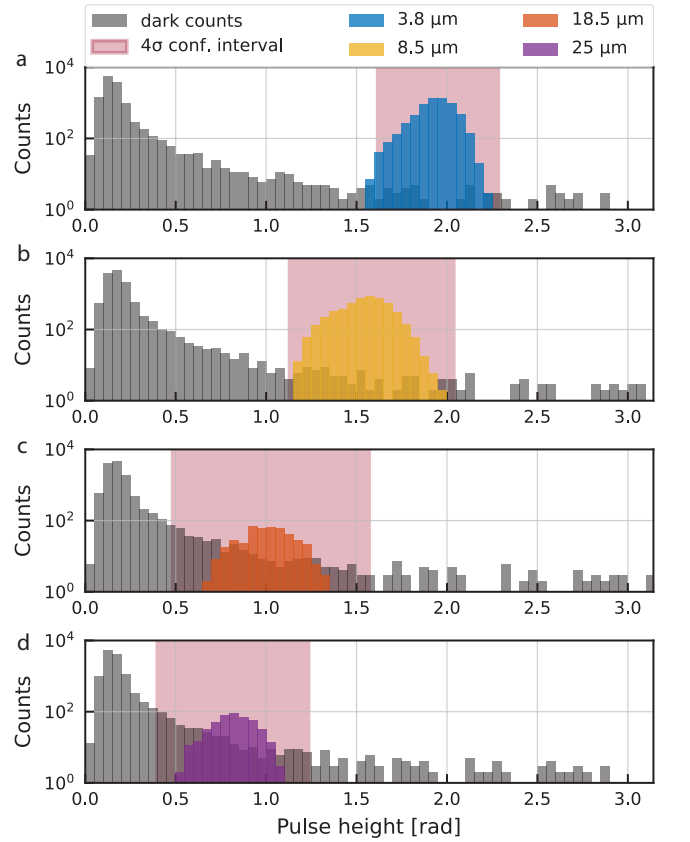


FIG. 9. Dark count analysis at 3.8, 8.5, 18.5 and 25 μm (panels a-d, respectively). The dark counts (gray shaded) were obtained during a 10000s dark measurement and optimally filtered using the noise from the dark measurement and the pulse templates per wavelength as also used for Fig. 4. The dark count rate per wavelength is determined from the overlap of the dark counts with the direct single-photon pulse distributions (blue, yellow, orange and purple shaded in top to bottom panels, respectively; from Fig. 4 and scaled with  $Q_1^{\text{dark}}$ ). The filled, red area represents the 99.73% ( $\mu \pm 4\sigma$  or  $\bar{H} \pm 1.7\delta H$ ) confidence interval of selecting all the direct single-photon pulses.

- [2] National Academies of Sciences, Engineering, and Medicine and others, *Pathways to Discovery in Astronomy and Astrophysics for the 2020s* (Washington, DC: The National Academies Press., 2023).
- [3] V. P. Bailey, E. Bendek, B. Monacelli, C. Baker, G. Bedrosian, E. Cady, E. S. Douglas, T. Groff, S. R. Hildebrandt, N. J. Kasdin, *et al.*, Nancy Grace Roman Space Telescope coronagraph instrument overview and status, *Techniques and Instrumentation for Detection of*

- Exoplanets XI **12680**, 283 (2023).
- [4] J. E. Hylan, M. R. Bolcar, J. Crooke, G. Bronke, C. Collins, J. Corsetti, J. Generie, Q. Gong, T. Groff, W. Hayden, A. Jones, B. Matonak, L. Sacks, G. West, K. Yang, N. Zimmerman, and S. Park, The large uv/optical/infrared surveyor (luvoir): Decadal mission concept study update, in *2019 IEEE Aerospace Conference* (2019) pp. 1–15.
  - [5] B. S. Gaudi, S. Seager, B. Mennesson, A. Kiessling, K. Warfield, K. Cahoy, J. T. Clarke, S. Domagal-Goldman, L. Feinberg, O. Guyon, *et al.*, The Habitable Exoplanet Observatory (HabEx) mission concept study final report, arXiv preprint arXiv:2001.06683 <https://doi.org/10.48550/arXiv.2001.06683> (2020).
  - [6] L. Simard, The Thirty-Meter Telescope: science and instrumentation for a next-generation observatory, *Journal of Astrophysics and Astronomy* **34**, 97 (2013).
  - [7] J. L. Codona, Exoplanet imaging with the Giant Magellan Telescope, in *Advancements in Adaptive Optics*, Vol. 5490 (SPIE, 2004) pp. 379–388.
  - [8] M. Kasper, N. C. Urra, P. Pathak, M. Bonse, J. Nouisainen, B. Engler, C. T. Heritier, J. Kammerer, S. Leveratto, C. Rajani, *et al.*, PCS—a roadmap for Exoearth Imaging with the ELT, arXiv preprint arXiv:2103.11196 [10.18727/0722-6691/5221](https://doi.org/10.18727/0722-6691/5221) (2021).
  - [9] METIS Consortium *et al.*, METIS: The Mid-infrared ELT Imager and Spectrograph, *The Messenger* **182**, 22 (2021).
  - [10] S. P. Quanz, M. Ottiger, E. Fontanet, J. Kammerer, F. Menti, F. Dannert, A. Gheorghe, O. Absil, V. S. Airapetian, E. Alei, *et al.*, Large interferometer for exoplanets (LIFE)-I. improved exoplanet detection yield estimates for a large mid-infrared space-interferometer mission, *Astronomy & Astrophysics* **664**, A21 (2022).
  - [11] F. A. Dannert, M. Ottiger, S. P. Quanz, R. Laugier, E. Fontanet, A. Gheorghe, O. Absil, C. Dandumont, D. Defrère, C. Gascón, *et al.*, Large interferometer for exoplanets (LIFE)-II. signal simulation, signal extraction, and fundamental exoplanet parameters from single-epoch observations, *Astronomy & Astrophysics* **664**, A22 (2022).
  - [12] L. Kaltenegger, How to characterize habitable worlds and signs of life, *Annual Review of Astronomy and Astrophysics* **55**, 433 (2017).
  - [13] B. Konrad, E. Alei, S. Quanz, D. Angerhausen, Ó. Carrión-González, J. Fortney, J. L. Grenfell, D. Kitzmann, P. Mollière, S. Rugheimer, *et al.*, Large Interferometer For Exoplanets (LIFE)-III. spectral resolution, wavelength range, and sensitivity requirements based on atmospheric retrieval analyses of an exo-earth, *Astronomy & Astrophysics* **664**, A23 (2022).
  - [14] T. L. Roellig, C. McMurtry, T. Greene, T. Matsuo, I. Sakon, and J. Staguhn, Mid-infrared detector development for the Origins Space Telescope, *Journal of Astronomical Telescopes, Instruments, and Systems* **6**, 041503 (2020).
  - [15] G. G. Taylor, A. B. Walter, B. Korzh, B. Bumble, S. R. Patel, J. P. Allmaras, A. D. Beyer, R. O’Brien, M. D. Shaw, and E. E. Wollman, Low-noise single-photon counting superconducting nanowire detectors at infrared wavelengths up to 29  $\mu\text{m}$ , *Optica* **10**, 1672 (2023).
  - [16] B. Hampel, D. Kuznesof, A. S. Mueller, S. R. Patel, R. H. Hadfield, E. E. Wollman, M. D. Shaw, D. Schwarzer, A. M. Wodtke, K. Hossain, *et al.*, Tungsten germanide single-photon detectors with saturated internal detection efficiency at wavelengths up to 29  $\mu\text{m}$ , arXiv preprint arXiv:2511.20868 <https://doi.org/10.48550/arXiv.2511.20868> (2025).
  - [17] J. A. Lau, V. B. Verma, D. Schwarzer, and A. M. Wodtke, Superconducting single-photon detectors in the mid-infrared for physical chemistry and spectroscopy, *Chemical Society Reviews* **52**, 921 (2023).
  - [18] S. Dello Russo, A. Elefante, D. Dequal, D. K. Pallotti, L. Santamaria Amato, F. Sgobba, and M. Siciliani de Cumis, Advances in mid-infrared single-photon detection, in *Photonics*, Vol. 9 (MDPI, 2022) p. 470.
  - [19] G. Huber, M. Bottom, C.-A. Claveau, S. Jacobson, M. Newland, I. Baker, K. Barnes, and M. Hicks, Glow reduction of ultra-low noise LmAPDs: towards photon counting infrared arrays, in *X-Ray, Optical, and Infrared Detectors for Astronomy XI*, Vol. 13103 (SPIE, 2024) pp. 780–788.
  - [20] P. D. Anderson, J. D. Beck, W. Sullivan III, C. Schaake, J. McCurdy, M. Skokan, P. Mitra, and X. Sun, Recent advancements in HgCdTe APDs for space applications, *Journal of Electronic Materials* **51**, 6803 (2022).
  - [21] G. Gol’tsman, O. Okunev, G. Chulkova, A. Lipatov, A. Semenov, K. Smirnov, B. Voronov, A. Dzardanov, C. Williams, and R. Sobolewski, Picosecond superconducting single-photon optical detector, *Applied physics letters* **79**, 705 (2001).
  - [22] P. K. Day, H. G. LeDuc, B. A. Mazin, A. Vayonakis, and J. Zmuidzinas, A broadband superconducting detector suitable for use in large arrays, *Nature* **425**, 817 (2003).
  - [23] P. K. Day, N. F. Cothard, C. Albert, L. Foote, E. Kane, B. H. Eom, R. Basu Thakur, R. M. Janssen, A. Beyer, P. M. Echternach, *et al.*, A 25-micrometer single-photon-sensitive kinetic inductance detector, *Physical Review X* **14**, 041005 (2024).
  - [24] M. Calvo, A. Benoit, A. Catalano, J. Goupy, A. Monfardini, N. Ponthieu, E. Barria, G. Bres, M. Grollier, G. Garde, *et al.*, The nika2 instrument, a dual-band kilopixel kid array for millimetric astronomy, *Journal of Low Temperature Physics* **184**, 816 (2016).
  - [25] A. Endo, K. Karatsu, Y. Tamura, T. Oshima, A. Taniguchi, T. Takekoshi, S. Asayama, T. J. Bakx, S. Bosma, J. Bueno, *et al.*, First light demonstration of the integrated superconducting spectrometer, *Nature Astronomy* **3**, 989 (2019).
  - [26] N. Reyes, A. Weiss, S. Yates, A. Baryshev, S. Endo, L. Ferrari, A. Görlitz, G. Grutzeck, R. Güsten, C. Heiter, *et al.*, Amkid—a large kid-based camera at the apex telescope, arXiv preprint arXiv:2512.14905 [10.48550/arXiv.2512.14905](https://doi.org/10.48550/arXiv.2512.14905) (2025).
  - [27] A. B. Walter, N. Fruitwala, S. Steiger, J. I. Bailey, N. Zobrist, N. Swimmer, I. Lipartito, J. P. Smith, S. R. Meeker, C. Bockstiegel, *et al.*, The mkid exoplanet camera for subaru scexao, *Publications of the Astronomical Society of the Pacific* **132**, 125005 (2020).
  - [28] S. O. Dabironezare, G. Conenna, D. Roos, D. Lamers, D. P. Capelo, H. M. Veen, D. J. Thoen, V. Anvekar, S. J. Yates, W. Jellema, *et al.*, Lens based kinetic inductance detectors with distributed dual polarised absorbers for far infra-red space-based astronomy, arXiv preprint arXiv:2506.03359 [10.1109/TTHZ.2025.3610552](https://doi.org/10.1109/TTHZ.2025.3610552) (2025).
  - [29] B. A. Mazin, Superconducting materials for microwave kinetic inductance detectors, in *Handbook of Supercon-*

- ductivity* (CRC Press, 2022) pp. 756–765.
- [30] K. Kouwenhoven, D. Fan, E. Biancalani, S. A. De Rooij, T. Karim, C. S. Smith, V. Murugesan, D. J. Thoen, J. J. Baselmans, and P. J. De Visser, Resolving power of visible-to-near-infrared hybrid  $\beta$ -Ta/Nb-Ti-N kinetic inductance detectors, *Physical Review Applied* **19**, 034007 (2023).
- [31] P. J. De Visser, S. A. De Rooij, V. Murugesan, D. J. Thoen, and J. J. Baselmans, Phonon-trapping-enhanced energy resolution in superconducting single-photon detectors, *Physical Review Applied* **16**, 034051 (2021).
- [32] N. Swimmer, W. H. Clay, N. Zobrist, and B. A. Mazin, Characterizing the dark count rate of a large-format MKID array, *Optics Express* **31**, 10775 (2023).
- [33] T. O. Klaassen, M. C. Diez, C. Smorenburg, K. J. Wildeman, J. H. Blok, and G. Jakob, Optical Characterization of Absorbing Coatings for Sub-millimeter Radiation, in *Twelfth International Symposium on Space Terahertz Technology*, edited by I. Mehdi (2001) p. 400.
- [34] K. Kouwenhoven, *Visible to Near-Infrared Kinetic Inductance Detectors*, Ph.D. thesis, TU Delft (2024).
- [35] C. E. Tucker and P. A. Ade, Thermal filtering for large aperture cryogenic detector arrays, in *Millimeter and Submillimeter Detectors and Instrumentation for Astronomy III*, Vol. 6275 (SPIE, 2006) pp. 239–247.
- [36] M. S. Khalil, M. Stoutimore, F. Wellstood, and K. Osborn, An analysis method for asymmetric resonator transmission applied to superconducting devices, *Journal of Applied Physics* **111**, 10.1063/1.3692073 (2012).
- [37] S. Probst, F. Song, P. A. Bushev, A. V. Ustinov, and M. Weides, Efficient and robust analysis of complex scattering data under noise in microwave resonators, *Review of Scientific Instruments* **86**, 10.1063/1.4907935 (2015).
- [38] L. Swenson, P. Day, B. Eom, H. Leduc, N. Llombart, C. McKenney, O. Noroozian, and J. Zmuidzinas, Operation of a titanium nitride superconducting microresonator detector in the nonlinear regime, *Journal of Applied Physics* **113**, 10.1063/1.4794808 (2013).
- [39] The Scipy community, `scipy.signal.find_peaks`, [https://docs.scipy.org/doc/scipy/reference/generated/scipy.signal.find\\_peaks.html](https://docs.scipy.org/doc/scipy/reference/generated/scipy.signal.find_peaks.html) (2026), accessed: 2026-02-25.
- [40] A. Szymkowiak, R. Kelley, S. Moseley, and C. Stahle, Signal processing for microcalorimeters, *Journal of Low Temperature Physics* **93**, 281 (1993).
- [41] K. D. Irwin, *Phonon-mediated particle detection using superconducting tungsten transition-edge sensors*, Ph.D. thesis, Stanford University (1995).
- [42] A. Kozorezov, A. Volkov, J. Wigmore, A. Peacock, A. Poelaert, and R. Den Hartog, Quasiparticle-phonon downconversion in nonequilibrium superconductors, *Physical Review B* **61**, 11807 (2000).
- [43] N. Rando, A. Peacock, A. Van Dordrecht, C. Foden, R. Engelhardt, B. Taylor, P. Gare, J. Lumley, and C. Pereira, The properties of niobium superconducting tunneling junctions as x-ray detectors, *Nuclear Instruments and Methods in Physics Research Section A: Accelerators, Spectrometers, Detectors and Associated Equipment* **313**, 173 (1992).
- [44] M. Kurakado, Possibility of high resolution detectors using superconducting tunnel junctions, *Nuclear Instruments and Methods in Physics Research* **196**, 275 (1982).
- [45] E. J. Wollack, G. Cataldo, K. H. Miller, and M. A. Quijada, Infrared properties of high-purity silicon, *Optics Letters* **45**, 4935 (2020).
- [46] Y. Yao, A. J. Hoffman, and C. F. Gmachl, Mid-infrared quantum cascade lasers, *Nature Photonics* **6**, 432 (2012).
- [47] K. Karatsu, S. Mima, S. Oguri, J. Choi, R. T. Damayanthi, A. Dominjon, N. Furukawa, H. Ishino, H. Ishitsuka, A. Kibayashi, *et al.*, Development of microwave kinetic inductance detector for cosmological observations, *IEICE Transactions on Electronics* **98**, 207 (2015).
- [48] Tydex, Thz materials, [https://www.tydexoptics.com/products/thz\\_optics/thz\\_materials/](https://www.tydexoptics.com/products/thz_optics/thz_materials/) (2026), accessed: 2026-02-25.
- [49] I. A. Kaplunov, A. I. Kolesnikov, G. I. Kropotov, and V. E. Rogalin, Optical Properties of Single-Crystal Germanium in the THz Range, *Optics and Spectroscopy* **126**, 271 (2019).
- [50] I. A. Kaplunov, G. I. Kropotov, V. E. Rogalin, and A. A. Shakhmin, Optical properties of some crystalline fluorides in the terahertz region of the spectrum, *Optical Materials* **115**, 111019 (2021).
- [51] A. Deneuville, D. Tanner, and P. Holloway, Optical constants of ZnSe in the far infrared, *Physical review B* **43**, 6544 (1991).